ORIGINAL PAPER

Experimental studies of the flow-front and drag forces exerted by subaqueous mudflow on inclined base

Zainul Faizien Haza · Indra Sati Hamonangan Harahap · Lema Mosissa Dakssa

Abstract Submarine slides are one of the most complex geotechnical problems causing serious damages to the seabed environment. Damages may lead to imminent destruction of offshore facilities such as platform and subsea pipeline. Mud sediment was the most susceptible of subsea material involved in the event. The completeness of field investigation is very limited; therefore, laboratory experiment is implemented in view of modeling the dynamics movement at the time of submarine slides occurs. The current experiment was conducted by generating the mudflow in water ambient over an inclined base to observe the flow-front structures of the mudflow. As facility to investigate the drag force exerted by mudflow, additional pipe model was positioned at certain flow distance. Mud models were prepared from mixtures of 10–35 % by weight of kaolin and water. Mudflow observations were limited to 3.5-m run-out distance with an exemption for 35 % KCC since this percentage stopped flow at 2.3-m flow distance. The role analysis of destructive flow was developed by the determination of drag force coefficient exerted by mudflow incorporating the Reynolds number. Velocity analysis indicates that all flows were defined as initial flow since they have only one phase of slumping phase. With respect to head-flow height and densimetric Froude number, the general form of velocity propagation formula provided the satisfactorily results in tracing mudflow velocity observation of laboratory experiment. Furthermore, the higher percentage of KCC exerted the higher drag force than the lower one.

Keywords Submarine slide · Mudflow · Kaolin clay · Head-flow height · Drag force · Drag force coefficient

Z. F. Haza (✉) · I. S. H. Harahap · L. M. Dakssa
Civil Engineering Department, Universiti Teknologi PETRONAS, Bandar Seri Iskandar,
31750 Tronoh, Perak Darul Ridzuan, Malaysia
e-mail: zainulfaiz@gmail.com

I. S. H. Harahap
e-mail: indrasati@petronas.com.my

L. M. Dakssa
e-mail: lamiboru@gmail.com

1 Introduction

The phenomenon of failures within the seafloor that cause the displacement of seabed sediments is well known as submarine slide, it is one of geo-hazards. It was a serious and complex problem in the marine field because it caused damages to the seabed environment and seafloor facilities. These events were normally (in geological time scale) occurred in many areas around the continental margin, including slope instability, mudflows, and gas hydrates. It has potential detrimental consequences against offshore installations such as fixed platforms, submarine pipelines, cables, and other seafloor installations (Nadim 2006; Hsu et al. 2008). For instance, in 1946, the Vancouver Island M7.3 earthquake caused a number of submarine failures that destroyed coastal facilities and sheared submarine cables (Mosher et al. 2004). Recently, several research and post-failure field observations have been conducted. One of the important characteristics derived from post-failure analysis data is that the submarine slides can reach very long run-out distance up to hundreds of kilometers on a gentle slope (Elverhoi et al. 2000; Hance 2003; Blasio et al. 2004; Bryn et al. 2005).

Unconsolidated clays were the main material of seabed sediment deposits, which after collapse transform into a finely mixture of clay and water having properties of a non-Newtonian liquid. This movement represented the most effective process of sediment transport from the shallow continental margin into the deep ocean (Blasio et al. 2004). Other result obtained from field analysis was the majority of submarine slides involved cohesive fine-grained material, that is, clays and silts (Hance 2003). Some researches characterized kaolin as the most predominant clay mineral contained in seafloor sediment (Fallick et al. 1993; Youn et al. 2006; Martín-Puertas et al. 2007). That was in line with the findings that in terrigenous clastic sediment, muddy material dominated the schematic of sediment deposits (Nichols 1999).

Currently, direct field studies can only be performed as the post-event observation. Technical information of initiation and motion when submarine slide took place is very limited. Therefore, the program of experimental laboratory is designed. Several laboratory experiments have been conducted in order to investigate this phenomenon of submarine slide. For example, an experiment was performed as laboratory simulation on relative mobility of muddy subaqueous and subaerial debris flows using a mixture of materials consisting of water, kaolin, silt, and sand in certain percentage (Mohrig et al. 1999). This addressed comparison results of run-out distance between subaqueous debris flows and their subaerial counterparts that having similar rheology.

The current experimental work was carried out in view of providing the basis for developing methods regarding the investigation of initial mudflow of submarine slides. The aim of this research was to investigate the subaqueous mudflow along an inclined channel by focusing on the flow-front structures formation and drag forces exerted by the flow on pipeline. Results described in this work were intended to elaborate the dynamics of the front part of the flow in terms of velocity, the form of moving mass, and the collision event between mudflow and pipeline. Owing to the fact that clay was a material mostly contained in sediment deposits even as the main material in every submarine slide event (Hance 2003), the current experiment was limited for using mud only (without any other material, such as sand and gravel).

2 Background and literature review

Almost all previous experiments of subaqueous flow were conducted by implementing flume experiment with slurry material as mixture of clay and granular (i.e. sand and gravel)

(Mohrig et al. 1999; Ilstad et al. 2004; Elverhøi et al. 2005, 2010; Zakeri et al. 2008). However, by taking into consideration that mud has been the main material in submarine slides, it has inference that materials rich in clay were the most susceptible, even though there is no sediment deposit which contains clay only (as there are always sand and other coarse material contents). In order to eliminate the effect of coarse material, the current experiment was designed to study the flow behavior of mud as material of mixture of a very fine grain and water.

In mudflows, there is no time for excess pore water dissipation because the rate of movement is fast enough. The mechanics of this movement cannot be adequately explained by soil mechanics principles alone. As a result, applying fluid mechanics principles is necessary (Locat and Lee 2000). According to these principles, the analysis of flow behavior of submarine slide can be more appropriately studied using the gravity flow concept of fluid mechanics.

Gravity flow concept has been widely used in research on fluid flow with two phases of different density (Hallworth and Huppert 1998; Lentz and Helfrich 2002; Amy et al. 2005). They addressed results of densities effects, speed of gravity current along the slope, and abrupt transitions between high viscosity fluids with the less one. Furthermore, a simple technique to generate gravity flow has been named 'lock-exchange system' was commonly used, which basically means separating two types of fluids having different densities in two chambers by vertical barrier. Then, the barrier is removed suddenly to let the denser fluid flow along the chamber's base. This method has been used in several fluid experiments including studies on fluid density factor (Shin et al. 2004; Lowe et al. 2005; Birman et al. 2007) in which the effect of density ratio of two fluids has been investigated. Those methods were adopted in the current study by generating a mudflow in ambient water using a lock-exchange system with gravity flow concept.

The use of fluid mechanics approach accommodates the additional effect of flow plasticity on the drag force related to the dynamic pressure which is proportional to mud density and the squared flow velocity (Bruschi et al. 2006). Therefore, drag force generated by mudflow on pipe stem can be expressed by traditional fluid dynamic force and rheology properties of non-Newtonian fluid flow as the following equation (Pazwash and Robertson 1975).

$$F_{\mathrm{d}} = \frac{1}{2} \cdot \rho_{\mathrm{f}} \cdot C_{\mathrm{d}} \cdot A \cdot u^2 \tag{1}$$

where F_{d} is the drag force components perpendicular to pipe axis, ρ_{f} is the mud density, C_{d} is the drag force coefficient, A is area of pipe stem which is facing opposite to mudflow direction, and u is flow-front velocity of mudflow.

3 Experimental design

3.1 Mud model material and rheological properties

Mud model used in this experiment was made from a mixture of kaolin and water with percentage variation of kaolin clay content (hereinafter abbreviated as KCC) in range 10–35 %, with 5 % increment. Refined kaolin used was fabricated by the local kaolin industry of Malaysia. The specific gravity (GS) value of the kaolin clay is about 2.6. Kaolinite has a low shrink-swell capacity and a low-cation-exchange capacity (1–15 meq/100 g.), and it is soft and earthy.

Table 1 Mud mix design of kaolin clay and water proportion

Percentage of kaolin clay content (KCC) (%)	Kaolin		Water		Mud (l)
	Weight (kg)	Volume (l)	Weight (kg)	Volume (l)	
10	4.5	1.7	45	45	46.7
15	6.5	2.5	43	43	45.5
20	8.5	3.2	42	42	45.2
25	10.5	4	42	42	46
30	12.5	4.8	41	41	45.8
35	14	5.3	40	40	45.3

Each experiment used a fixed volume of 45 l of mud. Mixing process was done based on the weight of either kaolin or water. The density of kaolin used in mix design was 2,630 kg/m^3, while water 1,000 kg/m^3. Table 1 lists the mix design to produce 45 l of mud approximately.

Rheological tests, including density and viscosity, were carried out by using common equipment in oil and gas industry, Fann Model 35 Viscometer and Mud Balance Model 140. This equipment was used primarily in the stage of drilling in the oil wells exploration process. The instruments and test kits were designed to conform to the testing standards established by the American Petroleum Institute (API) and published in API SPEC 10, API RP 10B-2, API SPEC 13A, API RP 13B-1, 13B-2, 13D, 13I, 13J, and 13K, and they were suitable for field and laboratory uses. In order to complete and verify the rheology test results, mud models were re-tested using Brookfield Digital Viscometer DV-I+ equipment, according to ASTM D2196 (Standards 2005).

Related to handling of slurry material, condition of time-dependency process was monitored carefully as the slurry turns out to be rheopectic—a condition in which fluid viscosity increases with time (Coussot 1997; Zakeri et al. 2008). Therefore, manual stirring was continued until the apparatus of rheological test and laboratory experiment were ready to start.

3.2 Laboratory equipment of mudflow experiment

The facility for the laboratory implementation was designed and assembled at Hydraulics Laboratory of Universiti Teknologi PETRONAS, Malaysia. The main equipment was a rectangular channel of 8.53 m length, 0.25 width, and heights of 0.7 and 1.30 m at the beginning and the end point, respectively. Overall, channel was made of clear glass, including the base. It has an adjustable horizontal position for the sloping base setting. The chain-block elevator was used to adjust the channel base slope by lifting the beginning edge of channel until reaching the expected slope (see Fig. 1). In the current experiment, the slope angle used was 3°. It referred to field data that stated the highest frequency density distribution of the average angle of the slope at failure for the seafloor slope failures to be in the range of 3°–4° (Hance 2003).

The current experiment was basically intended to simulate the slump of mud, sliding into a pool of water then flowing over the surface of channel base. Figure 2 shows the scheme of experiment setup using respective rectangular channel. Channel was divided into two main parts (i.e. chambers): the mud and the water. A vertical barrier (hereinafter referred to as gate) separated the chambers. The section of 1 m along the base from
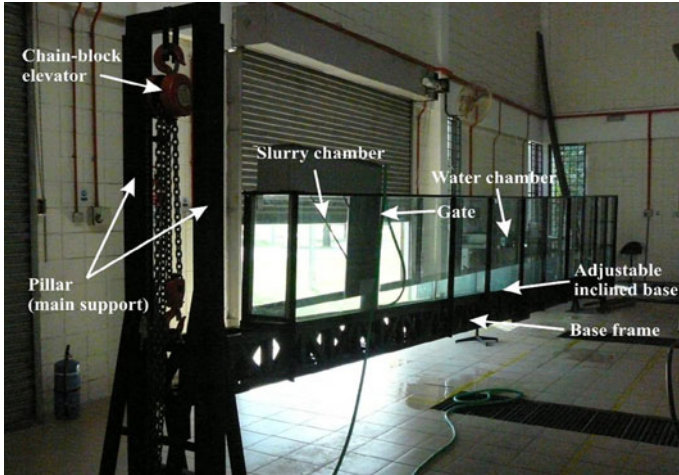
Fig. 1 Laboratory equipment of rectangular glass channel, framed by angle steel bar

sidewall until the gate was occupied by the mud, and then the water occupied the remaining section from gate until the end. The removable gate was pulled upward to let the mud start flowing into the water.

Instrumentation devices of experiment were four fixed cameras to record the movement of mudflow and to measure the head-flow velocity from the gate to the distance of 3.5 m as shown in Fig. 2. The most front camera, positioned at 0.5 m from gate, was Fujifilm FinePix J10 8.2mp (here was set as 2,304 × 1,728 pixels frame size). It was used to record the initiation of flow after gate opening. Other cameras were three cameras of Sony Handycam HDR-HC-7e 6mp that were positioned with a distance of 100 cm sequentially after the first camera. All three cameras were set in the same pixels frame size with the first camera in order to get comparable image quality.
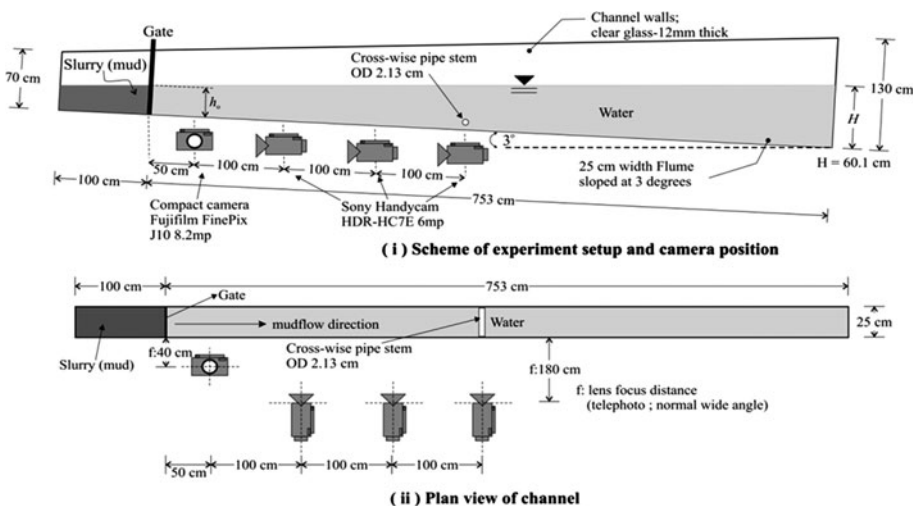

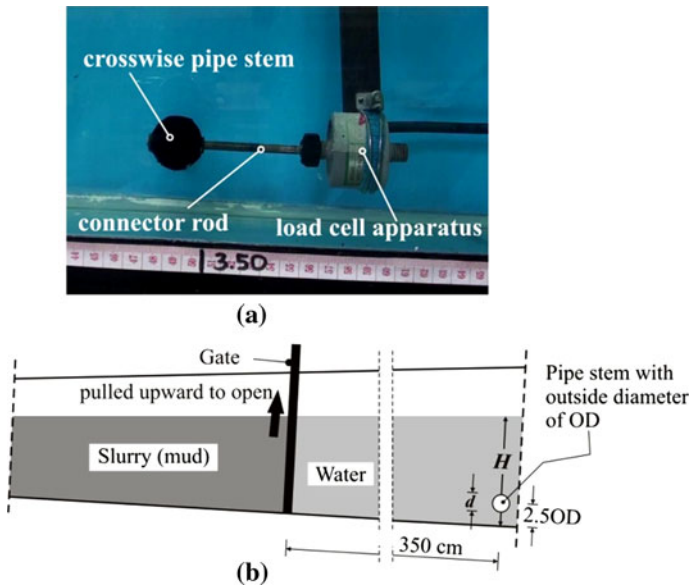**Fig. 2** Scheme of channel setup in mudflow experiment (not to scale)

Fig. 3 a Pipe load cell connection; **b** Scheme of pipe model position

3.3 Drag force measurement devices

The assembly of pipe model of outside diameter (OD) 2.13 cm and measurement devices are shown in Fig. 3. The pipe model was connected to load cell by steel bar (i.e. connector rod). The current setup was using load cell type of DDEN-250N-RS485 with environmental protection of IP68 to 10 m depth. A data logger device of '*Smart Dynamic Strain Recorder*' SDSR of DC-204R series was used to record the force responses of the load cell, which represented the force generated during collision between mudflow and pipe model.

The connector rod has a diameter of 8 mm, whose strength provided a rigid connection between load cell and pipe. Hence, the condition was in line with the assumption of experiment on drag force of mudflow on pipeline that there was no pipe deflection during collision. The position of pipe model and load cell arrangement was restrained by strip steel bar with thickness of 1.1 cm. Overall, the connection between all parts of the system was considered as rigid configuration, and there was no change position of pipe and load cell in either horizontal or vertical direction.

4 Result and discussion

4.1 Rheological properties

The rheology of clay–water mixture is possible to fit the experimental values in a wide shear rate ranges including values as small as 0.01 per second (or 0.01 s^{-1}) into the Herschel–Bulkley model (*H–B* model). It also provides a theoretical yield stress which is very close to real yield stress, with a low level of uncertainty for conventional practical application (Coussot 1997). Even though the linear viscoplastic Bingham model is the most commonly used to describe rheology of debris or mudflow, the *H–B* model has been found

to be more appropriate for describing the nonlinear viscoplastic behavior of debris flows (Balmforth et al. 2002; Cohard and Ancey 2009). Therefore, in the current study, H–B model was adopted to characterize the mud rheological behavior and it is expressed as in the following equation.

$$(\tau - \tau_c) = K \cdot \dot{\gamma}^n \tag{2}$$

where, τ_c is the yield strength, K is equivalent to the dynamic viscosity, $\dot{\gamma}$ is the shear rate, and n is positive parameters of model factor (Coussot 1997).

Various values of $\dot{\gamma}$ are determined from Brookfield Digital Viscometer DV-I+ apparatus including spindles and glass tube of mud sample. According to operation manual book, the uses of suitable spindles for the current test are type of RV#2 (for 10–20 % of KCC), RV#3 for 25 % of KCC, and RV#4 (for 30 and 35 % of KCC). Based on these spindles, values of $\dot{\gamma}$ are determined and plotted as a function of the linear velocity (u) of test execution, as shown in Fig. 4.

Rheological test results are listed in Table 2 as well as the equation of H–B model of the mud according to percentage of KCC. Table 2 represents the propagation of density magnitudes among material models based on percentage of KCC and its rheological model. Fann Mud Balance results values of mud densities in range of 1,054–1,266 kg/m^3. Furthermore, according to Table 2, H–B model shows the increment of yield strength (τ_c) in the range 0.6–9.0 Pa.

According to rheological test series, τ values of each percentage KCC at certain $\dot{\gamma}$ are obtained and plotted in a graph with $\dot{\gamma}$ as a function of τ. Solver of least squares approach of curve fitting method is employed to generate the fitting curve equation with approximation error as expressed as follows:

$$\text{err} = \sum_{i=1}^{N} \left(\tau_i - (\tau_{ci} + K_i \cdot \dot{\gamma}_i^n) \right)^2 \tag{3}$$

where N is the number of variation values of $\dot{\gamma}$ applied in test. In the current test, N has value of 8, according to number of spindle RPM of Brookfield Digital Viscometer DV-I+ equipment. By using data listed in Table 2, H–B model (Eq. 2) and laboratory results of the shear stress, characteristics of mud model are then presented in the graph of shear rate ($\dot{\gamma}$) versus shear stress (τ) as shown in Fig. 5.

Figure 5 shows that H–B model are fitting laboratory tests very well even for low applied shear rate test with R^2 in range of 98.9–99.6 %. Table 2 together with Fig. 5 indicates that the mud models properties are probably best described as non-Newtonian pseudo-plastic fluid with shear rate increases and they are exhibiting thixotropic shear thinning.
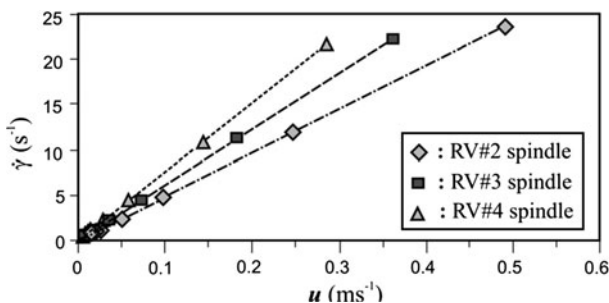

Fig. 4 Values of shear rate ($\dot{\gamma}$) based on linear velocity (u) applied on Brookfield test

Table 2 Rheological test results of mud for each percentage of KCC and H–B model	KCC (%)	Density (ρ_f)		Specific gravity (GS)	H–B model
		(lbs/gal)	(kg/m³)		
	10	8.79	1,054	1.07	$\tau = 0.6 + 0.73\dot{\gamma}^{0.3}$
	15	9.10	1,092	1.10	$\tau = 1.71 + 1.63\dot{\gamma}^{0.27}$
	20	9.45	1,134	1.13	$\tau = 3.4 + 4.73\dot{\gamma}^{0.32}$
	25	9.60	1,152	1.20	$\tau = 3.57 + 8.88\dot{\gamma}^{0.4}$
	30	10.30	1,236	1.23	$\tau = 5.7 + 12.68\dot{\gamma}^{0.42}$
	35	10.55	1,266	1.27	$\tau = 9 + 20.36\dot{\gamma}^{0.5}$

4.2 Overview of laboratory experiment

The experiment was tracking the movement of mudflow by applying timeline feature (t), front velocity of head-flow (u), and run-out distance (l). The velocity of the mudflow as a function of flow-time and run-out distance was the main data, so that the track record of velocity data in the analysis of laboratory experiments was the reference point in the elaboration and examination of other flow aspects.

Observation was made by referring to gravity flow concepts that describe the phenomena of stratified fluids when a denser fluid body spread under a less dense body of fluid (Mok et al. 2003). Furthermore, Mok et al. provided the advance sketch of the typical gravity current front in 2D view as shown in Fig. 6.

Mudflow was initiated by gate opening. Once the gate was pulled over, the mud was collapsed and it was immediately forming the gravity flows because of two factors: mud density and slope of channel base. The gravity flow has the basic characteristic shape of gravity currents: head, body, and tail structure. This current study was focusing on the characteristic of head-flow. Referring to Fig. 6, head-flow is the front part of flow including nose (the most front) until lobes' area with height of h, whereas lobes are shapes characterized by relatively small humps which are emerged after head-flow. The mudflow body has thickness (t_h), which has approximation value as a half of the total height of head-flow (h) (Ieong et al. 2006). The mudflow body thickness as well as billows is part of
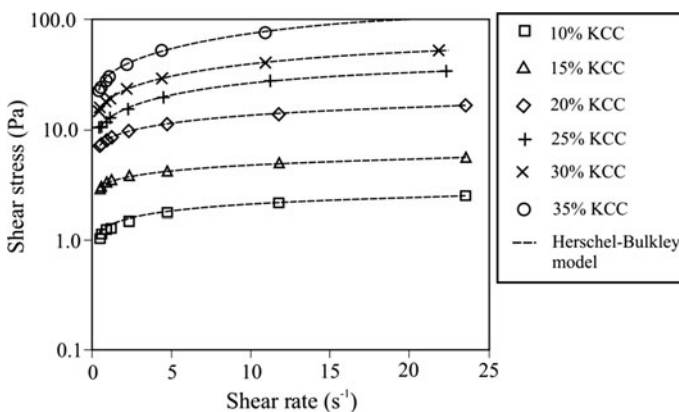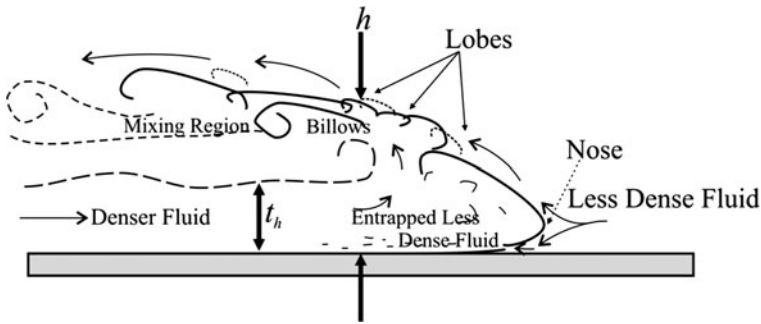

Fig. 5 Mud rheological test and H–B model fit

Fig. 6 Sketch of a typical gravity current front and its particular sections (modified from (Mok et al. 2003))

mudflow, which is very difficult to make a visual observation by camera alone; hence, these parts are not further discussed. The mixing region is area behind the lobes indicated by swirling light clumps of mud particle and water mixture (i.e. eddies) with reverse motion direction against mudflow.

For all percentage of KCC, laboratory experiment was repeatedly performed by three times in order to obtain the typical and comparable of flow attributes of certain percentage. Flow attributes are flow-front velocity, head-flow height, run-out distance, and water depth at nose position. Data used in the analysis were the average data among those experiments. Figure 7 shows the example of images in sequential views of 15 % KCC mudflow, which was made by arranging the compilation of captured video.

The body shape of mudflow is in conformity with sketch of typical gravity current (see Fig. 6) in terms of performing the main visual indicators of gravity current (i.e. nose, head, lobes, and mixing region) as the event when the denser fluid intruded into less dense fluid. The chaotic interaction of flow regime on interface of mud and water is representing the mixing region of the mudflow.

A very small wave in water surface was generated by the motion of mudflow; however, this phenomenon was not observed further since the water surface was definitely free surface condition, which was considered that it has no significant effect to the flow. The measurement and analysis of physical data obtained from the movement during flow comprising of run-out distance (l), flow-front velocity (u), and height of the head-flow (flow-front height, h) will be discussed in the following section.

4.3 Flow measurement

Sketch drawings were made at $t = 0$ (initial condition) and at $t > 0$ (i.e. during moving or flow) in order to facilitate the observations and measurements. Figure 8 sketches the details of particular identification of mudflow at the start and during flow condition. In the initial condition ($t = 0$), the height (h_0) and the length (l_0) of mud deposit were measured as 20.64 cm and 100 cm, respectively (Fig. 8a). At flow condition, besides time (t), height of head-flow (h), water depth (H), and run-out distance (l) were recorded (Fig. 8b).

The head-flow heights (h) can be tracked during motion in accordance with run-out distance (l) based on sequential image capture as similar as shown in Fig. 7 and referring to Fig. 8 to assign the point of measurement position. During flow, not only measurable flow attributes as shown in Fig. 8 but also physical attributes of densities and non-dimensional
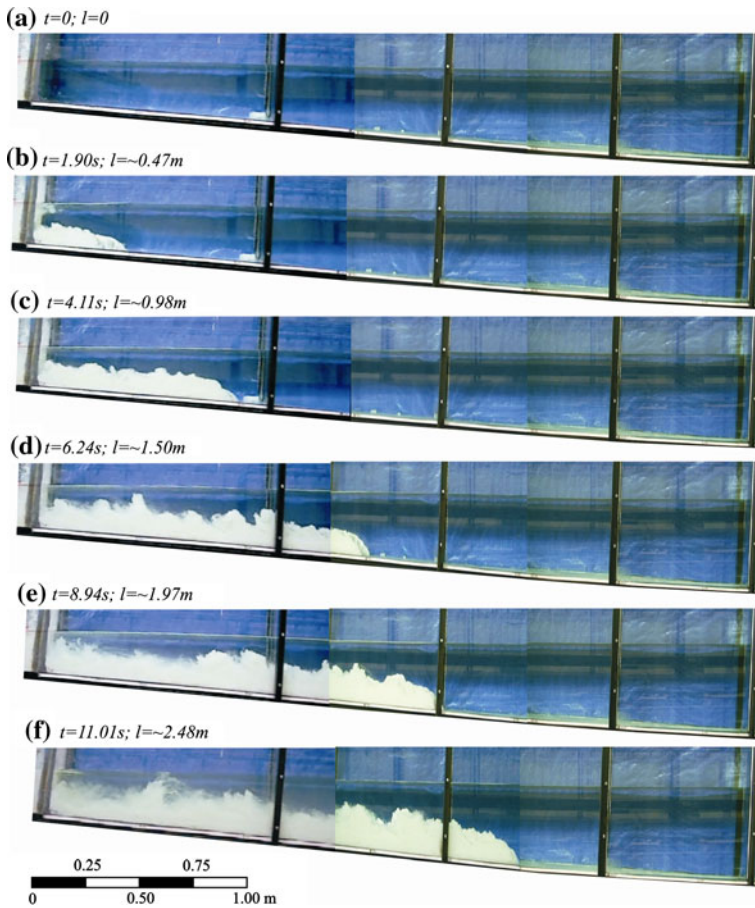
Fig. 7 Sequential views of captured images of mudflows formation of 15 % KCC; from $l = 0$ to $l = \sim 2.51$ m; from $t = 0$ to $t = 11.01$ s

numbers were analyzed. Those were density ratio ($\rho_r = \rho_w/\rho_f$), initial density ratio (ρ_i), Reynolds number (R_e), and densimetric Froude number (F_r). In the scope of fluid mechanics, previous research differentiated fluid flow behavior in two types: based on the reduced gravity of g'' formulated as $g'' = g \, (\rho_f - \rho_w)/\rho_f$, and g' formulated as $g' = g \, (\rho_f - \rho_w)/\rho_w$ (Hallworth and Huppert 1998; Lowe et al. 2005; Amy et al. 2005; Rotunno et al. 2011). As found in the previous works (Hallworth and Huppert 1998; Amy et al. 2005), that adopting g'' was not sufficiently conformed between theory and experiments for high concentration fluid, where the levels of fluid concentration are referred to initial density ratio, ρ_i, which is formulated as the following.

$$\rho_i = \{(\rho_f - \rho_w) / (\rho_f + \rho_w)\}^{1/2} \tag{4}$$

where for $\rho_i > 0.3$ was considered as high concentration fluid. By referring to Table 3, the values of ρ_i are varying in range of 0.17–0.34. This gap is encompassing low and a bit high concentration level. Since g'' was reported having insufficient application for high concentration, in this experiment analysis, the reduced gravity of g' was applied instead of g''.
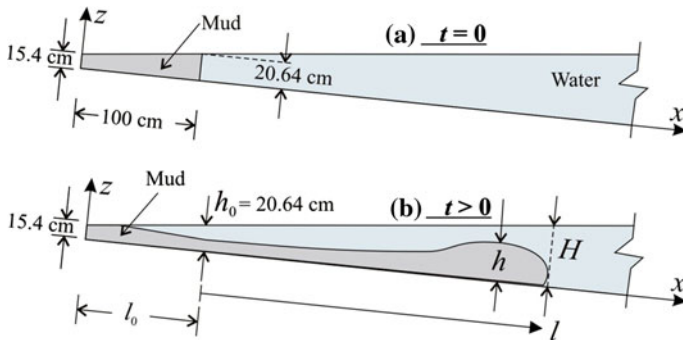
Fig. 8 Schematic of subaqueous mudflow at $t = 0$ and $t > 0$

The non-dimensional numbers (Reynolds number, R_e, and densimetric Froude number, F_r) calculation was implemented by determining the viscosity apparent (μ_{app}), which was obtained by dividing the shear stress, τ, by shear rate, $\dot{\gamma}$ as proposed by (Zakeri et al. 2008).

$$\mu_{app} = \frac{\tau_c}{\dot{\gamma}} + K \cdot \dot{\gamma}^{n-1} \tag{5}$$

The Reynolds number formulation presented as Eq. (6). It is composed by components of the μ_{app} together with ρ_f, u, and $\dot{\gamma}$.

$$R_{e(non-Newtonian)} = \frac{\rho_f \cdot u^2}{\mu_{app} \cdot \dot{\gamma}} \tag{6}$$

The densimetric Froude number of the mudflow is calculated by the following equation (Mohrig et al. 1999), where θ is the slope angle.

$$F_r = \frac{u}{\sqrt{\left(\frac{\rho_f}{\rho_w} - 1\right)gh\cos\theta}} = \frac{u}{\sqrt{g'h\cos\theta}} \tag{7}$$

According to laboratory setup and numbers of percentage of KCC, Table 3 presents the list of initial conditions and experimental measurement results.

Table 3 indicates that the mudflow with high value of τ_c and μ_{app} generated the low value of R_e during motion. The laboratory experiments are confirming the fluid mechanics principles that fluid flow tends to become turbulent when the value of R_e is higher. This turbulence is indicated by more chaotic flow surface. Figure 9 shows the example of chaotic flow surface of mudflow of 10–30 % KCC.

Figure 9 represents the typical flow regime in the current study, which shows the mudflows mixing region of all percentage of KCC. It shows that mudflow with low percentage of KCC relatively generated more chaotic interactions surface between mud and water.

4.4 Flow-front velocity

The occurrence velocity of the mudflow is not uniform on the entire body of flowing mass. Each part of mudflow mass (see Fig. 6) has different velocity magnitude. Therefore, the current study was using term of 'flow-front velocity' to represent the velocity of the

Table 3 Initial condition of experiment and measurement results ($l_0 = 100$ cm; $h_0 = 20.64$ cm)

Mud model	ORP (m)	ρ (kg/m³)	ρ_i	ρ_r	l (m)	t (s)	u (m/s)	h (m)	H (m)	R_e	F_r
10 % KCC ~ 0.5	0.5	1,054	0.162	0.949	0.51	2.12	0.240	0.07	0.233	65.69	1.249
10 % KCC ~ 1	1.0	1,054	0.162	0.949	0.99	5.04	0.164	0.11	0.258	30.68	0.682
10 % KCC ~ 1.5	1.5	1,054	0.162	0.949	1.52	8.24	0.166	0.17	0.286	65.69	0.552
10 % KCC ~ 2.0	2.0	1,054	0.162	0.949	2.02	11.26	0.166	0.19	0.312	31.43	0.522
10 % KCC ~ 2.5	2.5	1,054	0.162	0.949	2.5	13.26	0.240	0.2	0.337	65.69	0.739
10 % KCC ~ 3	3.0	1,054	0.162	0.949	2.98	14.99	0.278	0.24	0.363	88.14	0.780
10 % KCC ~ 3.5	3.5	1,054	0.162	0.949	3.47	16.71	0.285	0.25	0.388	92.64	0.782
15 % KCC ~ 0.5	0.5	1,092	0.210	0.916	0.47	1.90	0.248	0.07	0.231	25.26	0.922
15 % KCC ~ 1	1.0	1,092	0.210	0.916	0.98	4.11	0.230	0.1	0.258	21.89	0.768
15 % KCC ~ 1.5	1.5	1,092	0.210	0.916	1.5	6.24	0.244	0.16	0.285	24.53	0.642
15 % KCC ~ 2.0	2.0	1,092	0.210	0.916	1.97	8.94	0.174	0.17	0.310	12.52	0.445
15 % KCC ~ 2.5	2.5	1,092	0.210	0.916	2.48	11.01	0.246	0.19	0.336	25.02	0.595
15 % KCC ~ 3	3.0	1,092	0.210	0.916	3.01	13.14	0.249	0.22	0.364	25.52	0.559
15 % KCC ~ 3.5	3.5	1,092	0.210	0.916	3.5	15.12	0.248	0.23	0.390	25.26	0.544
20 % KCC ~ 0.5	0.5	1,134	0.251	0.882	0.5	1.14	0.439	0.07	0.233	39.20	1.447
20 % KCC ~ 1	1.0	1,134	0.251	0.882	1.03	3.33	0.242	0.08	0.260	11.91	0.745
20 % KCC ~ 1.5	1.5	1,134	0.251	0.882	1.47	5.80	0.179	0.13	0.283	6.52	0.432
20 % KCC ~ 2.0	2.0	1,134	0.251	0.882	2	7.99	0.242	0.15	0.311	11.91	0.544
20 % KCC ~ 2.5	2.5	1,134	0.251	0.882	2.5	9.95	0.255	0.16	0.337	13.22	0.557
20 % KCC ~ 3	3.0	1,134	0.251	0.882	3.03	12.06	0.251	0.19	0.365	12.81	0.503
20 % KCC ~ 3.5	3.5	1,134	0.251	0.882	3.54	13.93	0.274	0.21	0.392	15.27	0.521
25 % KCC ~ 0.5	0.5	1,152	0.266	0.868	0.5	1.14	0.439	0.07	0.233	22.67	1.359
25 % KCC ~ 1	1.0	1,152	0.266	0.868	1.05	3.36	0.248	0.1	0.261	7.24	0.641
25 % KCC ~ 1.5	1.5	1,152	0.266	0.868	1.53	5.13	0.271	0.12	0.287	8.64	0.642
25 % KCC ~ 2.0	2.0	1,152	0.266	0.868	2	7.01	0.250	0.14	0.311	7.35	0.548
25 % KCC ~ 2.5	2.5	1,152	0.266	0.868	2.49	9.04	0.256	0.15	0.338	7.71	0.543

Table 3 continued

Mud model	ORP (m)	ρ (kg/m³)	ρ_i	ρ_r	l (m)	t (s)	u (m/s)	h (m)	H (m)	R_e	F_r
25 % KCC ~ 3	3.0	1,152	0.266	0.868	2.9	10.54	0.254	0.16	0.358	7.59	0.520
25 % KCC ~ 3.5	3.5	1,152	0.266	0.868	3.5	12.85	0.259	0.17	0.390	7.89	0.515
30 % KCC ~ 0.5	0.5	1,236	0.325	0.809	0.48	1.17	0.410	0.08	0.232	16.30	0.953
30 % KCC ~ 1	1.0	1,236	0.325	0.809	1	3.47	0.226	0.09	0.259	6.45	0.496
30 % KCC ~ 1.5	1.5	1,236	0.325	0.809	1.47	5.51	0.230	0.1	0.283	9.75	0.478
30 % KCC ~ 2.0	2.0	1,236	0.325	0.809	1.98	8.33	0.181	0.1	0.310	4.14	0.377
30 % KCC ~ 2.5	2.5	1,236	0.325	0.809	2.51	10.00	0.317	0.09	0.338	5.13	0.694
30 % KCC ~ 3	3.0	1,236	0.325	0.809	3	11.94	0.253	0.09	0.364	8.08	0.554
30 % KCC ~ 3.5	3.5	1,236	0.325	0.809	3.5	13.93	0.251	0.09	0.390	7.95	0.551
35 % KCC ~ 0.5	0.5	1,266	0.343	0.790	0.54	1.25	0.431	0.08	0.235	13.10	0.944
35 % KCC ~ 1	1.0	1,266	0.343	0.790	0.98	3.76	0.175	0.07	0.258	2.11	0.411
35 % KCC ~ 1.5	1.5	1,266	0.343	0.790	1.52	5.97	0.226	0.08	0.284	3.60	0.496
35 % KCC ~ 2.0	2.0	1,266	0.343	0.790	1.98	15.86	0.051	0.08	0.310	0.18	0.111
35 % KCC ~ 2.5	2.5	1,266	0.343	0.790	2.51	–	–	–	–	–	–
35 % KCC ~ 3	3.0	1,266	0.343	0.790	2.51	–	–	–	–	–	–
35 % KCC ~ 3.5	3.5	1,266	0.343	0.790	2.51	–	–	–	–	–	–

ORP observation reference point; the points with certain distance from gate as data reference
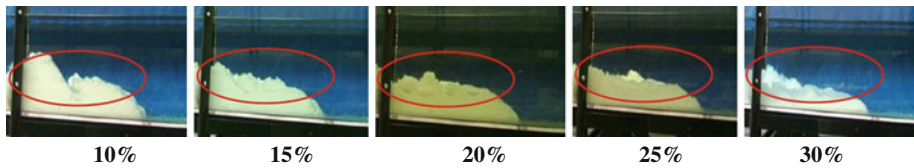
| 10% | 15% | 20% | 25% | 30% |

Fig. 9 Examples of the chaotic flow surface (i.e. mixing region) of mudflow at $l = 2.5$ m with percentage of 10–30 % KCC (see the area bordered by *ellipse line*)
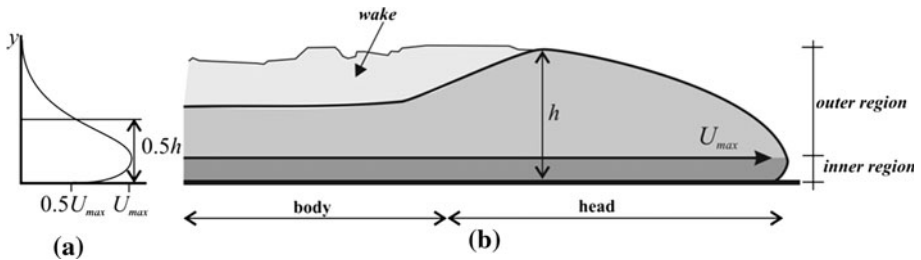

Fig. 10 a Velocity profile of the flow **b** Anatomy of subaqueous debris flow [modified from (Kneller and Buckee 2000)]

mudflow. Estimating the maximum velocity reached by flow was implemented by referring to (Kneller and Buckee 2000) which described the velocity profile diagram of subaqueous debris flow.

In Fig. 10, the nose is exhibiting the position of maximum velocity path of the flow. Hence, the nose position along x-axis is appropriately used as indicator and the reference for determination of velocity (u) and run-out distance (l).

Investigation of flow-front velocity (u) was implemented by introducing the ORP (see Table 3) to facilitate the observation of velocity propagation. Velocity magnitudes are determined by dividing the distance between two consecutive ORPs with respective measured time. While the measured time is the duration time taken by the leading edge of slurries head (i.e. nose) to flow between two consecutive ORPs. The propagation of the flow-front velocities starting from gate point until 3.5 m of run-out is shown in Fig. 11.

Figure 11 represents the flow behaviors of the mudflow in terms of velocity at certain run-out distance, which shows the fluctuations including acceleration and deceleration. In the range of $l_{1.0}$ to $l_{3.5}$ run-out distance, each mud model of 10–30 % KCC has a relative small velocity fluctuation, whereas 35 % KCC is undergone a rapid deceleration to stop at around $l_{2.3}$. These results are observed by referring to Table 2 that 35 % KCC has the highest τ_c, which leads the flow resistance against continuous flow and causes the short run-out distance at distance of about 2.3 m. In further, as the ratio between a characteristic velocity and a gravitational wave velocity (Eq. (7)), the values of densimetric Froude number (F_r) are indicating the effect of gravitational force. The higher percentage of KCC produced the lower value of F_r, thus the 35 % KCC (see Table 3) represents the high effect of gravitational forces, which is indicated by rapid deceleration.

The shear stress (τ) occurred in these flows can be observed by determination of the shear rate ($\dot{\gamma}$). Based on actual flow velocity calculation in Table 3, flow velocities are in range 0.164–0.439 m/s after 0.5 m of run-out. Referring to Fig. 4, this range of velocities is having $\dot{\gamma}$ values in the range of 7–34 s^{-1}; thus, the mudflows in the current experiment
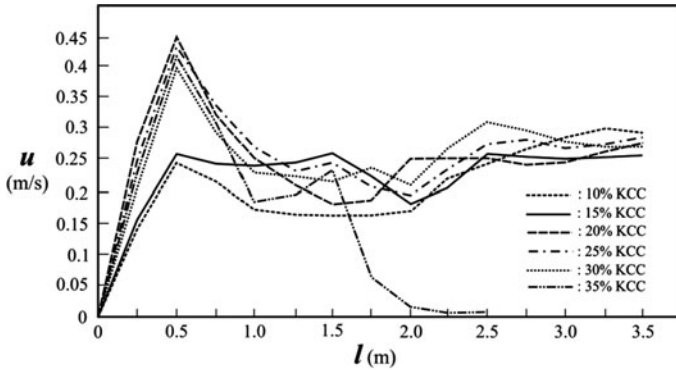
Fig. 11 Flow-front velocities as a function of run-out distance in the range of 0–3.5 m

are generating the minimum shear stress (τ_{min}) of 4.47 Pa and maximum (τ_{max}) of 127.72 Pa. The maximum shear stress was occurred at around ORP of 0.5 where the flows developed the highest acceleration as seen in Fig. 11. Values of $\dot{\gamma}$ produced by these flows are higher than $3\ s^{-1}$, which are appropriate with the range of interest for the flume experiments as stated by Zakeri et al. (2008).

The comparison study is referring to experiment conducted by Mohrig et al. (1999). As mentioned in the introduction, that experiment was conducted as a laboratory simulation on relative mobility of muddy subaqueous and subaerial debris flows using a mixture of materials consisting of water, kaolin, silt, and sand in certain percentage. By using ρ_f of 1,600 kg/m^3 and 6° of slope, the experiment delivered results as follows: values of u in the range of 0.48–0.65 m/s and F_r in the range of 1.9–2.47 (Mohrig et al. 1999). The flow-front velocity behavior was similar with current experiment that the flow also generated the flow-front velocity fluctuation. Overall, the comparison infers that ρ_f is the main factor in generating the head-flow velocity, whereas θ does not give a big effect since it has not a significant difference magnitude of $\cos\theta$ as expressed in Eq. (7).

Regarding flow measurement (elapsed time of flow, propagation velocities, and run-out distance), there are three flow phases in mudflow identification. Those are slumping phase, inertial-buoyancy phase, and viscous-buoyancy phase (Huppert and Simpson 1980; Rottman and Simpson 1983; Amy et al. 2005). Furthermore, Amy et al. provided a schematic of the change in gradient of the line indicate the phase transition as shown in Fig. 12.

Fig. 12 Schematic of the line gradient representing the three phases of flow (Amy et al. 2005)
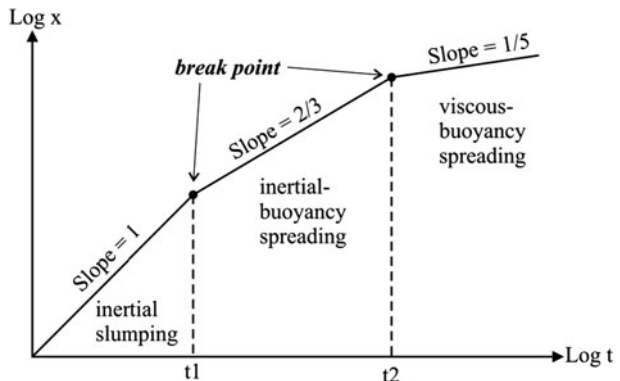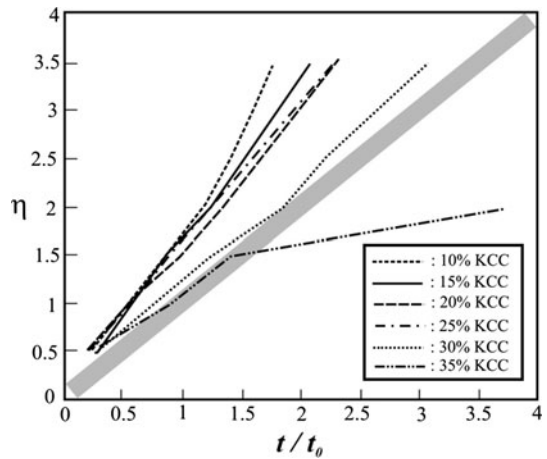
Fig. 13 Non-dimensional run-out distance (i.e. flow-front position) as a function of non-dimensional time for each percentage of KCC

In the current experiment, the position of flow-front was traced by plotting time (t) versus run-out distance (l) in order to relate the effect of velocity fluctuation on flow. The plotting graphs are implemented by introducing two non-dimensional parameters: length unit (η) and time unit (t/t_0). The length unit (η) is the normalization of l by l_0; thus, it is formulated as l/l_0, with respect to initial length of mud deposit, l_0, whereas the time unit (t/t_0) is formulated as $t_0 = l_0/(g'h_0)^{1/2}$ with respect to t_0. Figure 13 shows the plotting graph with axes of η and (t/t_0), which depicts the slope and break points of certain percentage of KCC.

The line of each percentage is not a straight line from beginning to the end point—there are some break points along the line. This condition indicates that the mudflow velocities are not linear, which are conforming to the graph of velocity fluctuations as shown in Fig. 11. The bold gray line in Fig. 13 is straight line and put in 45° slope. It assists the observation of the slope condition of [$\eta/(t/t_0)$]. Figure 13 shows only 35 % KCC that has part of line that is crossing the gray line. This line part has slope value of 0.185. Since the value is less than 1/5, it is defined viscous-buoyancy phase condition. Thus, Fig. 13 confirmed that only 35 % KCC has undergone two phases of slumping phase and viscous-buoyancy phase, whereas 10–30 % KCC have only undergone one phase of slumping phase, indicated by their lines, which are not crossing the gray line. It means that the lines are having slope value equal to 1 or larger. Therefore, all flows (except 35 % KCC) performed in this current experiment are considered as an initial flow since they have only one phase, in accordance with schematic of different types of current spreading pattern provided by Amy et al. (Amy et al. 2005). Since it is considered as slumping phase, the fluid density of head-flow portion is assumed similar with the original mud mixture up to 3.5 m of run-out distance. These assumptions are used for further investigation of drag forces exerted by mudflow along relatively short run-out distance, which involves density and velocity aspects.

4.5 Flow-front height

In reference to Fig. 8 and Table 3, it can be tracked during motion that the front height (h) of mudflow is increasing in accordance with run-out distance. The growth of h is a result of two distinct mechanisms between mud and water. Thereafter, the front heights listed in Table 3 are plotted in graph with axis of run-out distance as shown in Fig. 14.
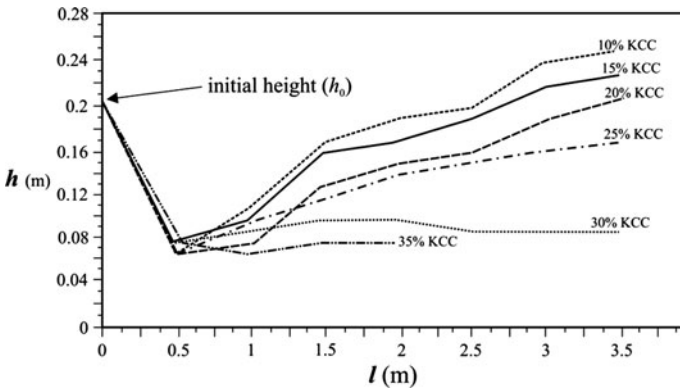
Fig. 14 Head-flow height, h, as a function of run-out distance l

Figure 14 shows the fluctuations of head-flow height. All mudflow models start an increment of head-flow height at range of 0.5 to 1 m of run-out distance. These increments are conforming to findings provided by Kneller et al. that body velocity of gravity flow is faster than head velocity (Kneller et al. 1997), hence the body motion amassed the mud in the head-flow portion. This condition leads the emergence of nose and increases the height of head-flow as well (see Fig. 10b). Moreover, the yield strength (τ_c) has a significant effect to the head-flow height increment. This can be observed by referring to Table 2 that the percentage increments of KCC (i.e. 10–35 %) obviously increase the τ_c, but, on the other hand, it reduce the height of head-flow (h).

In the case of head-flow height dynamics, observation has to incorporate aspects of velocity and density as the main factor of head-flow formation. In reference to (Middleton 1996 a) after (An 2011), the velocity propagation is defined as the following general form.

$$u = C\sqrt{g'h} \tag{8}$$

where C is defined as the coefficient related to fractional depth as the ratio of head-flow height and water depth (h/H). The value of C is also investigated based on inviscid-fluid theory and energy-conserving flow when expressed as the following equation (Benjamin 1968).

$$C = \left(\frac{(H-h)(2H-h)}{H(H+h)} \right)^{1/2} \tag{9}$$

Moreover, Banjamin concluded that C and (h/H) was inversely proportional that C was decreasing with increasing the (h/H), and the maximum value of C was obtained at (h/H) $\sim$ zero. A line (hereinafter named as C–h/H line) was used to express the general relation of C and (h/H). In the current experiment, by substitution data of h and H in Table 3 to Eq. (9), the correlation between C and (h/H) can be seen in Fig. 15.

As shown in Fig. 15, all percentage of KCC meet the Benjamin's identification regarding the correlation between C and h/H as they address values which are very close to C–h/H line. Some previous studies have proposed the values of C based on experiments of gravity currents formed by saline water. These researches have proposed the values of C as 0.75 and 0.76 (Middleton 1996 a; Keulegan 1957) after (An 2011). According to the structure and components of Eq. (8), it was equal to F_r equation as written in Eq. (7).
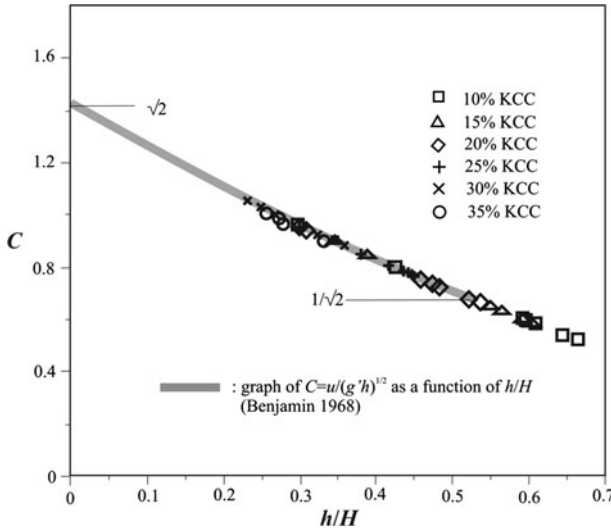
Fig. 15 Propagation values of *C* related to *h/H*; combined with *C–h/H* line proposed by Benjamin (Benjamin 1968)

Accordingly, Eq. (8) is then modified into the following equation in order to develop the general form of velocity profile of the current experiments with regard to *h*. The modified equations are as follows.

$$u = C\sqrt{g'h \cdot \cos\theta} \qquad (10)$$

$$C = k(F_r) \qquad (11)$$

where *k* is a coefficient of ratio between *C* and F_r. In order to obtain the suitable value of *k*, solver of least squares approach is employed. The solver provides results as listed in Table 4.

As in Table 3, F_r was calculated at every ORP. Similarly, the values of *k* are verified by implementing the calculation of the propagation of mudflow velocities (*u*) using modified velocity equation of Eq. (10) at every ORP. Results obtained from the calculation are compared to laboratory experiment data of mudflow velocities in Table 3. Results are also plotted into graph of *l* as a function of *u* as shown in Fig. 16.

Figure 16 shows the trends of mudflow velocity propagation of particular percentage of KCC in the experiment laboratory together with calculation result of modified velocity

Table 4 Values of *k* as the coefficient ratio between *C* and F_r according to %KCC

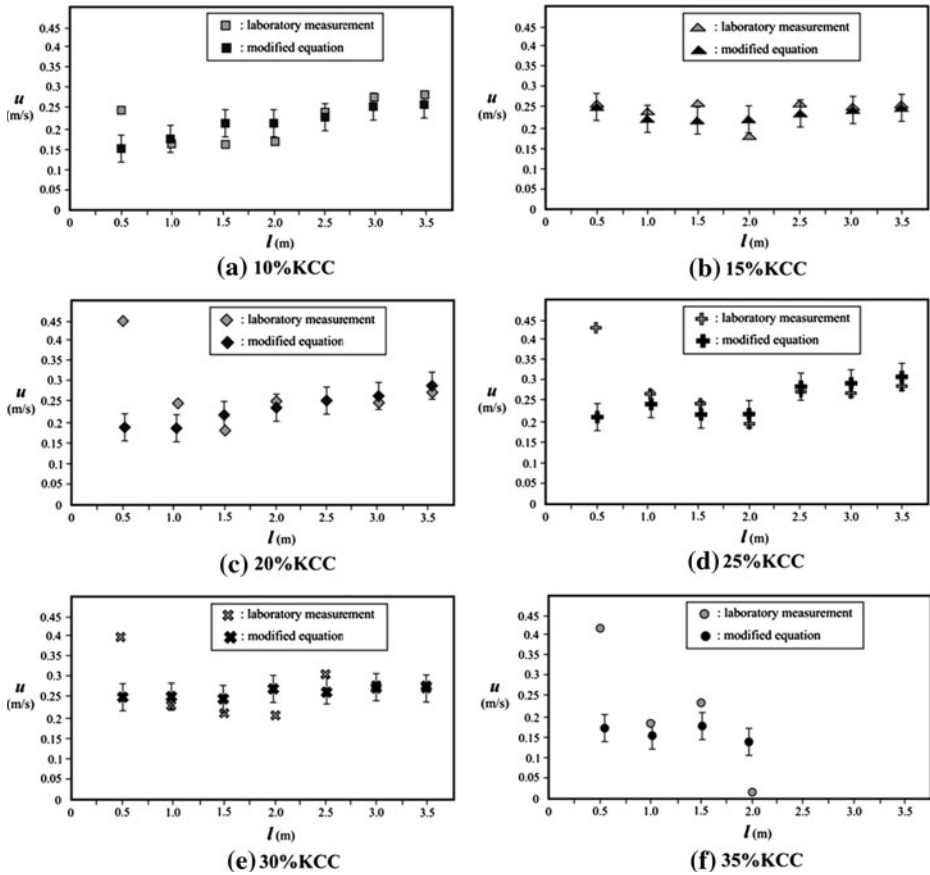| % KCC	k
10	1.02
15	0.91
20	0.94
25	0.93
30	1.02
35	1.22

**Fig. 16** Verification of mudflow velocity propagation using the modified velocity equation

equation. It confirms that both of modified velocity equation (Eq. (10)) and values of k in Table 4 are satisfactorily approaching the laboratory results.

4.6 Drag force coefficient

As mentioned in previous section, drag forces were measured upon the collision between mudflow and pipe model in laboratory experiment, whereas drag force coefficient (C_d) is determined based on the drag force exerted by mudflow (F_d). Figure 17 shows an example of the consecutive captured images of 15 % KCC mudflow upon collision against the pipe model.

The drag force magnitudes were acquired from signal responses provided by load cell, which were converted into force unit by data logger (see Fig. 3a). The conversion was still involving the noise signals, which cause inaccurate reading of force magnitude. Therefore, signal processing was implemented to obtain a precise reading of data logger output, which was performed through computational programming of MATLAB (Mathworks.Inc 2012). Tool of fast Fourier transform (FFT) was employed to analyze the data logger output. Measured data produced by data logger were time series of drag force (i.e. time domain

Fig. 17 Collision events of 15 % KCC mudflow against suspended pipe stem of OD 21.3 mm
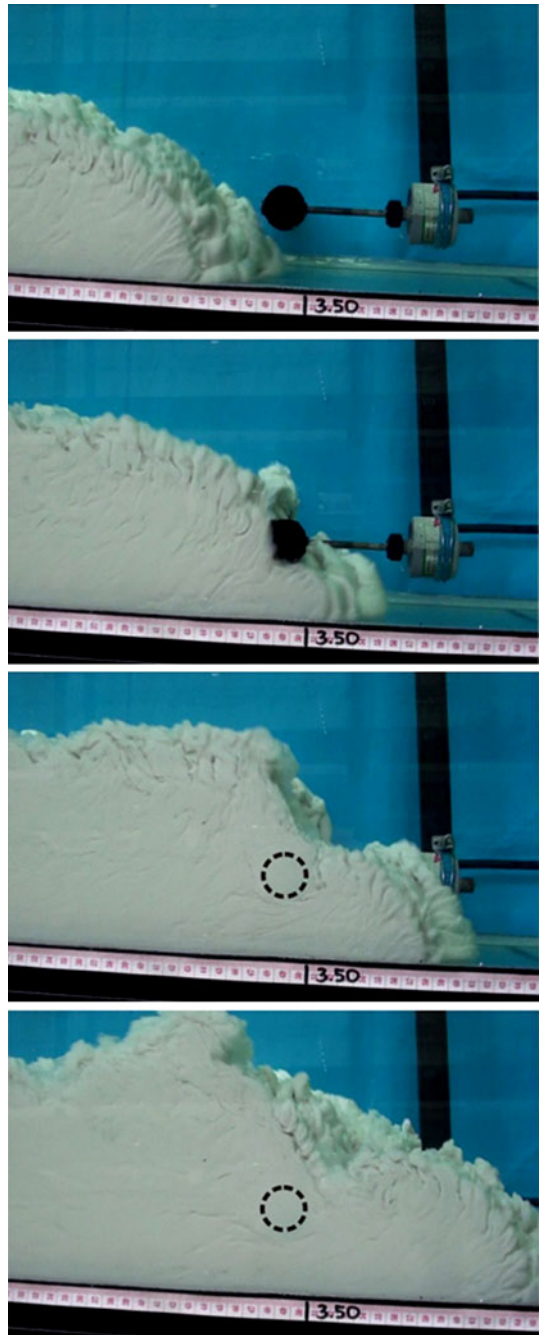
(a)

data). In principle, FFT algorithm implemented the discrete Fourier transform (DFT) to transform data from time domain into frequency domain in which the noise frequency can be determined.
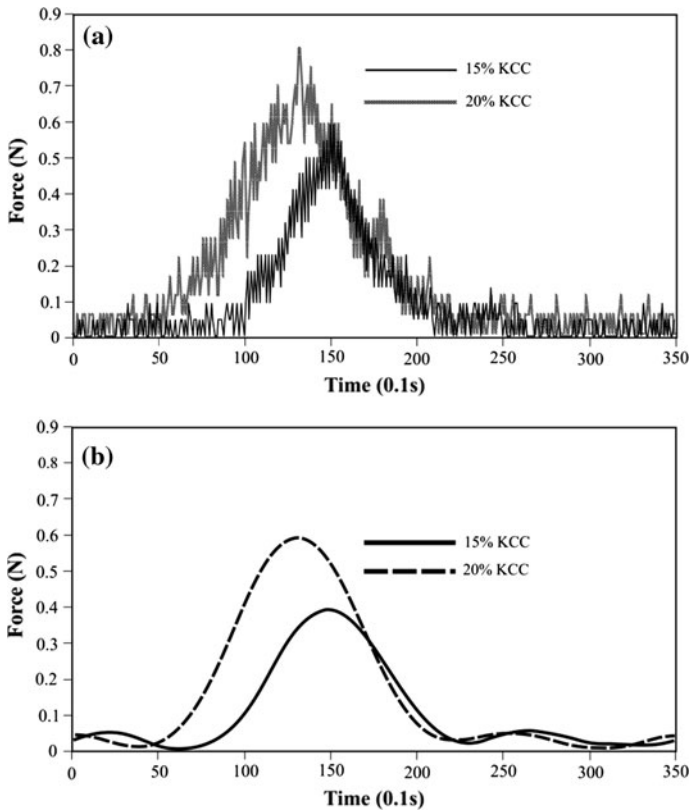
Fig. 18 Force responses of the pipe model; **a** data logger output; **b** FFT filter output

In this experiment, the noise signal was detected as in high frequency; therefore, 'the low-pass filter' was applied in analysis. Furthermore, based on noise signal spectrum, low-pass filter of 0.0114 Hz was applied as the threshold filter onto drag force data produced by data logger. Once the noise signal was removed from the output data, the actual drag force could be determined. Figure 18 shows an example of typical force responses of 15 and 20 % KCC recorded by data logger together with FFT filter result.

Figure 18b represents the actual drag force exerted by mudflow, which is not as high as data logger output. It is caused by the noise influence of load cell used in the system. As a compilation of the filtering process, Fig. 19 shows the typical responses of drag force exerted by mudflow for each percentage of KCC.

The maximum drag force of all current experiments as shown in Fig. 19 is in the range of 0.248–1.104 N. Coefficients of drag forces (C_d) are calculated based on the F_d maximum in order to observe the maximum impact of mudflow on pipe model. Calculation using Eq. (1) obtained the values of C_d in the range of 0.74–3.17 as presented in Table 5. Flow measurement and analysis results including drag force, drag force coefficient, and Reynolds number are listed in the same table.

Based on Table 5, an equation is then developed to express the C_d as relative to Reynolds number (R_e). The expression of $C_d - R_e$ relationship is as follows ($R^2 = 92.7$ %).
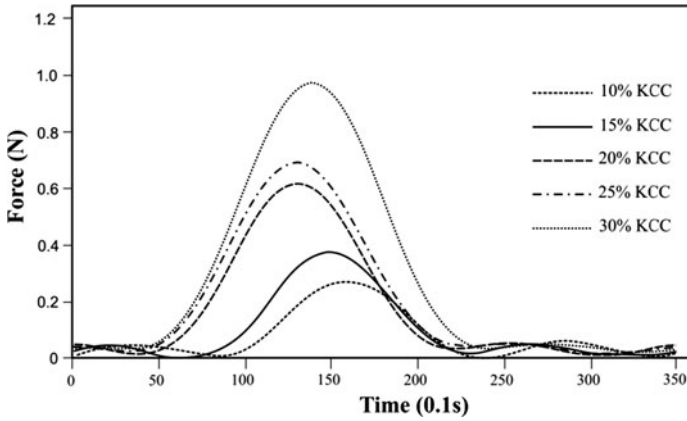
Springer

Fig. 19 FFT output of typical responses of drag force exerted by mudflow

Table 5 Flow-front velocities and collision analysis including Reynolds number, drag forces, and drag force coefficients

Mud model	ρ (kg/m³)	u (m/s)	R_e	$F_{d\ max}$ (N)	C_d
10 % KCC-3.5	1,054	0.285	92.64	0.267	0.74
15 % KCC-3.5	1,092	0.248	25.26	0.336	1.19
20 % KCC-3.5	1,134	0.274	15.27	0.515	1.44
25 % KCC-3.5	1,152	0.259	7.89	0.694	2.14
30 % KCC-3.5	1,236	0.251	7.95	1.038	3.17
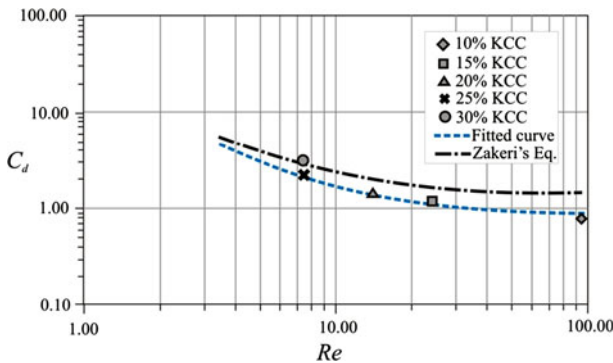
Fig. 20 Drag coefficient as relative to Reynolds number of laboratory experiment, fitted curve, and Zakeri's equation (Zakeri et al. 2008)

$$C_d = 0.7 + 29.1R_e^{(-1.3)} \tag{12}$$

The fitting formulation of this developed equation is presented in Fig. 20. In 2008, Zakeri et al. had proposed a correlation between C_d and R_e, which is expressed as $C_d = 1.4 + \frac{17.5}{R_{e\,non-Newtonian}^{1.25}}$, where C_d and $R_{e\ non-Newtonian}$ were drag force coefficient and Reynolds number, respectively. As mentioned, the experiment used slurry material as mixture of clay and granular (i.e. sand and gravel) with density in the range of 1,681–1,694 kg/m³

(Zakeri et al. 2008). The laboratory setup was different with the current experiment, which Zakeri et al. experiment did not use lock-exchange system, but slurries were supplied by head tank and flowed into water compartment through a chute. By using data of R_e in Table 5, Zakeri's equation is employed to calculate the C_d, which results also presented in Fig. 20.

The different values of C_d are appearing in graph between fitted curve result of laboratory experiment analysis and calculation result using formula proposed by Zakeri et al., even so both are showing the similar trend line. The high similarity trend line between two conditions of the current study and Zakeri's as shown in Fig. 20 indicates that kaolin clay content plays a major role in mudflow movement and collision characteristic, whereas granular material is only presenting an extra density for flowing mass.

5 Concluding remarks

Experimental work of subaqueous mudflow was performed to model the initial motion of mud sediment of submarine slides. It was implemented based on lock-exchange system and gravity flow concepts. Mud model was mixtures of kaolin and water (10–35 % of KCC) with densities in the range of 1,054–1,266 kg/m^3. The rheological properties were described satisfactorily using Herschel–Bulkley rheological model. The characteristics of mud were best described as non-Newtonian pseudo-plastic fluid with shear rate increases.

Flow-front velocities were fluctuating in the range of 0.164–0.439 m/s after 0.5 m of run-out; they induced the minimum and maximum shear stresses of 4.47 and 127.72 Pa, respectively. These motions produced the shear rate values from 7 to 34 s^{-1}. All flows (except 35 % KCC) have only one phase of slumping phase. It indicated that all flows were considered as initial flow, and head-flows portion could be assumed having density equal to the original mud mixture until 3.5 m of run-out distance.

With respect to the correlation between velocity propagation and head-flow height, presenting the coefficient k to densimetric Froude number (F_r) was suitable to define the C (coefficient related to fractional depth), that is $C = k$ (F_r), where k has values that varied from 0.91 to 1.22 for all percentages of KCC. The application of k values in the calculation of mudflow velocity propagation provided similar results with laboratory experiment.

Analysis of the collision between mudflows and OD 2.13-cm pipeline produced the maximum drag force was in the range of 0.248–1.104 N and obtained the values of drag force coefficient in the range of 0.74–3.17. Figures of drag force coefficient as a function of Reynolds number confirmed that kaolin clay content was playing a major role in mudflow movement and collision characteristic, whereas granular material was only an extra density of mass flow. It is indicated by high similarity of trend line between two conditions of the current study and past experiment, which used additional material of sand and gravel.

References

Amy LA, Hogg AJ, Peakall J, Talling PJ (2005) Abrupt transitions in gravity currents. J Geophys Res 110:1–19. doi:10.1029/2004JF000197,2005

An SD (2011) Interflow dynamics and three-dimensional modeling of turbid density currents in Imha reservoir, South Korea. Colorado State University, Fort Collins

Balmforth NJ, Craster RV, Sassi R (2002) Shallow viscoplastic flow on an inclined plane. J Fluid Mech 470:1–29. doi:10.1017/S0022112002001660

Benjamin TB (1968) Gravity currents and related phenomena. J Fluid Mech 31:209–248

Birman VK, Battandier BA, Meiburg E, Linden PF (2007) Lock-exchange flows in sloping channels. J Fluid Mech 577:53–77. doi:10.1017/S002211200600437X

Blasio FVD, Engvik L, Harbitz CB, Elverhøi A (2004) Hydroplaning and submarine debris flows. J Geophys Res 109:1–15. doi:10.1029/2002JC001714,2004

Bruschi R, Bughi S, Spinazze M, Torselletti E, Vitali L (2006) Impact of debris flows and turbidity currents on seafloor structures. Norw J Geol 86:317–337

Bryn P, Berg K, Forsberg CF, Solheim A, Kvalstad TJ (2005) Explaining the storegga slide. Mar Pet Geol 22:11–19

Cohard S, Ancey C (2009) Experimental investigation of the spreading of viscoplastic fluids on inclined plane. J Nonnewton Fluid Mech 158:73–84. doi:10.1016/j.jnnfm.2008.08.07

Coussot P (1997) Mudflow rheology and dynamics. AA Balkema, Rotterdam

Elverhøi A, Harbitz CB, Dimakis P, Mohrig D, Marl J, Parker G (2000) On the dynamics of subaqueous debris flows. Oceanography 13:109–117

Elverhøi A, Issler D, De Blasio FV, Ilstad T, Harbitz CB, Gauer P (2005) Emerging insights on the dynamics of submarine debris flows. Nat Hazards Earth Syst Sci 5:633–648

Elverhøi A, Breien H, De Blasio FV, Harbitz CB, Pagliardi M (2010) Submarine landslides and the importance of the initial sediment composition for run-out length and final deposit. Ocean Dyn Special Issue 60:1027–1046. doi:10.1007/s10236-010-0317-z

Fallick AE, Macaulay CI, Haszeldine RS (1993) Implications of linearly correlated oxygen and hydrogen isotopic compositions for kaolinite and illite in the magnus sandstone, North Sea. J Clays Clay Miner 41:184–190

Hallworth MA, Huppert HE (1998) Abrupt transitions in high-concentration, particle-driven gravity currents. Phys Fluids 10:1083–1087

Hance JJ (2003) Development of a database and assessment of seafloor slope stability based on published literature. The University of Texas, Austin

Hsu S-K, Kuo J, Lo C-L, Tsai C-H, Doo W-B, Ku C-Y, Sibuet J-C (2008) Turbidity currents, submarine landslides and the 2006 Pingtung earthquake off SWTaiwan. Terr Atmos Ocean Sci 19(6):767–772. doi:10.3319/TAO.2008.19.6.767(PT

Huppert HE, Simpson JE (1980) The slumping of gravity currents. J Fluid Mech 99:785–799

Ieong KK, Mok KM, Yeh H (2006) Fluctuation of the front propagation speed of developed gravity current. In: Conference of global Chinese scholars on hydrodynamics. Shanghai University Press, Shanghai, pp 351–355. doi:10.1016/S1001-6058(06)60077-2

Ilstad T, Blasio FVD, Elverhoi A, Harbitz CB, Engvik L, Longva O, Marr JG (2004) On the frontal dynamics and morphology of submarine debris flows. Mar Geol 213:481–497

Keulegan GH (1957) Thirteenth progress report on model laws for density currents an experimental study of the motion of saline water from locks into fresh water channels. U.S. Natl Bur Standards Rept

Kneller BC, Buckee CM (2000) The structure and fluid mechanics of turbidity currents: a review of some recent studies and their geological implications. Sedimentology 47(Suppl. 1):62–94

Kneller BC, Bennett SJ, McCaffrey WD (1997) Velocity and turbulence structure of gravity currents and internal solitary waves: potential sediment transport and the formation of wave ripples in deep water. Sed Geol 112:235–250

Lentz SJ, Helfrich KR (2002) Bouyant gravity currents along a sloping bottom in a rotating fluid. J Fluid Mech 464:251–278. doi:10.1017/S0022112002008868

Locat J, Lee HJ (2000) Submarine Landslides: Advances and Challenges. Paper presented at the 8th international symposium on landslides, Cardiff, June 2000

Lowe RJ, Rottman JW, Linden PF (2005) The non-Boussinesq lock-exchange problem. Part 1. Theory and experiments. J Fluid Mech 537:101–124. doi:10.1017/S0022112005005069

Martín-Puertas C, Mata MP, Fernández-Puga MC, Río VDd, Vázquez JT, Somoza L (2007) A comparative mineralogical study of gas-related sediments of the Gulf of Cádiz. Geo Marine Lett 27:223–235. doi:10.1007/s00367-007-0075-1

Mathworks. Inc (2012) http://www.mathworks.com/help/matlab/ref/fft.html. Accessed 20 June 2012

Middleton GV (1996) Experiments on density and turbidity currents: I. Motion of the head. Can J Earth Sci 3(5):627–637

Mohrig D, Elverhøi A, Parker G (1999) Experiments on the relative mobility of muddy subaqueous and subaerial debris flows, and their capacity to remobilize antecedent deposits. Mar Geol 154:117–129

Mok KM, Ieong KK, Yeh H (2003) Experimental Observations of the flow structures at gravity current fronts. Paper presented at the international conference on estuaries and coasts, Hangzhou, 9–11 Nov 2003

Mosher DC, Monahan PA, Barrie JV, Courtney RC (2004) Submarine failures in the strait of Georgia, British Columbia: landslide of the 1946 Vancouver Island earthquake. J Coast Res 20:277–291

Nadim F (2006) Challenges to geo-scientists in risk assessment for sub-marine slides. Norw J Geol 86:351–362

Nichols G (1999) Sedimentology and stratigraphy. Oxford

Pazwash H, Robertson M (1975) Forces on bodies in Bingham fluids. J Hydraul Res 13(1):35–55. doi: 10.1080/00221687509499719

Rottman JW, Simpson JE (1983) Gravity currents produced by instantaneous releases of a heavy fluid in a rectangular channel. J Fluid Mech 135:95–110. doi:10.1017/S0022112083002979

Rotunno R, Klemp JB, Bryan GH, Muraki DJ (2011) Models of non-Boussinesq lock-exchange flow. J Fluid Mech 675:1–26. doi:10.1017/jfm.2010.648

Shin JO, Dalziel SB, Linden PF (2004) Gravity currents produced by lock exchange. J Fluid Mech 521:1–34. doi:10.1017/S002211200400165X

Standards (2005) ASTM D2196-05 standard test methods for rheological properties of non-Newtonian materials by rotational (Brookfield type) Viscometer. ASTM international

Youn JS, Byun JC, Lee SH (2006) Sedimentary strata and clay mineralogy of continental shelf mud deposits in the East China Sea. Int J Oceans Oceanogr 1:183–194

Zakeri A, Høeg K, Nadim F (2008) Submarine debris flow impact on pipelines—Part I: Experimental investigation. Coast Eng 55(2008):1209–1218